Tau-cell-based Analog Silicon Retina with Spatio-Temporal Filtering and Contrast Gain Control

Prince Phillip, *Student Member, IEEE,* Kapil Jainwal, *Member, IEEE,*
André van Schaik, *Fellow, IEEE* and Chetan Singh Thakur, *Senior Member, IEEE*

***Abstract*—Developing precise artificial retinas is crucial because they hold the potential to restore vision, improve visual prosthetics, and enhance computer vision systems. Emulating the luminance and contrast adaption features of the retina is essential to improve visual perception and efficiency to provide an environment realistic representation to the user. In this paper, we introduce an artificial retina model that leverages its potent adaptation to luminance and contrast to enhance vision sensing and information processing. The model has the ability to achieve the realization of both tonic and phasic cells in the simplest manner. We have implemented the retina model using 0.18μm process technology and validated the accuracy of the hardware implementation through circuit simulation that closely matches the software retina model. Additionally, we have characterized a single pixel fabricated using the same 0.18μm process. This pixel demonstrates an 87.7-% ratio of variance with the temporal software model and operates with a power consumption of 369 nW.**

***Index Terms*—Neuromorphic circuits, Silicon retina, Adaptation, Tau-cells, Bio-inspired, Contrast gain control, Spiking.**

I. Introduction

Frame-based image sensors are commonly used in the majority of vision-based systems. These sensors offer several advantages, including a smaller pixel pitch and a high fill factor. Moreover, they employ double sampling techniques such as correlated double sampling (CDS) or delta-reset sampling (DRS) to effectively reduce fixed-pattern noise (FPN). However, these image sensors are very slow, as all pixels are read in each frame regardless of the dynamics of the scene. Due to the frame-based readout scheme, the bandwidth of the system gets wasted, and the imaging system cannot perform well in a highly dynamic scene. When a fast-moving object is to be detected, the frame rate has to be increased. However, this results in an increase in power dissipation and the amount of generated data. Mechanisms for detecting regions of interest can also be used; however, it comes at the cost of higher computation [1]–[3].

Biological vision sensors, on the other hand, operate in a fundamentally distinct manner, drawing inspiration from the biology of the retina. Within the biological retina, specialized photoreceptor cells (rods and cones) respond to changes in light intensity. When light strikes these cells, they undergo an electrochemical process that generates nerve impulses, or spikes, which are transmitted to interconnected neurons. Similarly, in artificial neuromorphic vision sensors, when the light intensity sensed by a pixel undergoes a significant change, it triggers a spike that is transmitted to its linked neurons. In this approach, the sent-out data is only from the pixels which are detecting an event in terms of intensity change beyond a threshold [4]–[10]. Hence, the transmission bandwidth is only consumed by the activated pixels. Because of the fast response, wide dynamic range, low latency, and effective in-sensor processing, bio-inspired vision sensors have become increasingly appealing in recent years [11]–[14].

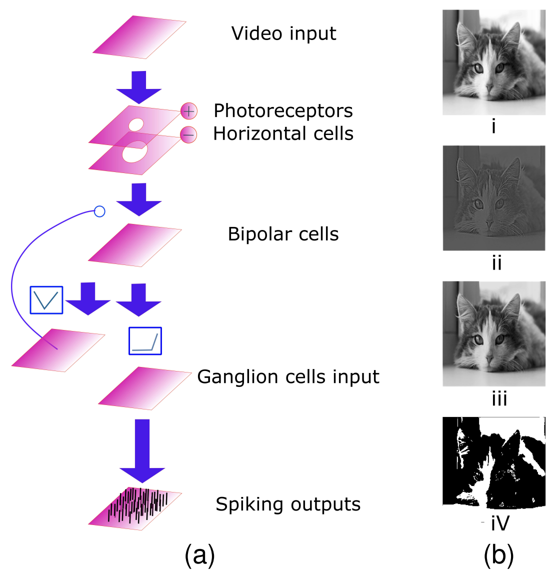

Fig. 1. (a) The analog circuit implementation of the retina is illustrated in a simplified diagram, starting with the photoreceptor cell that receives video input from the environment and ending with the spiking output from the ganglion cells; (b) Images are presented that demonstrate the impact of the stimulus on different layers of the retina model where the first image (i) displays a frame of the input video stimulus, while the second image (ii) depicts the effect of the OPL layer, represented by the difference of photoreceptors and horizontal cells in Fig. 1a, the third image (iii) shows the outcome of the bipolar layer, and the fourth image (iv) illustrates the resultant spiking activity.

Mahowald and Mead created the first silicon retina [4], which uses a diffuser grid to compute spatial contrast and includes photoreceptor cells, horizontal cells, and bipolar cells. Boahen and Andreou expanded on this approach by employ-

Prince Philip and Chetan Singh Thakur are with the Department of Electronic Systems Engineering, Indian Institute of Science, Bangalore, KA, 560012 INDIA (e-mail: princephilip@iisc.ac.in, csthakur@iisc.ac.in).
Kapil Jainwal is with the Department of Electrical Engineering, Indian Institute of Technology, Hyderabad, 502285, INDIA (email: kapiljainwal@ee.iith.ac.in).
André van Schaik is with the International Center for Neuromorphic Systems, The MARCS Institute for Brain, Behaviour and Development, Western Sydney University, Sydney, NSW 2751, AUSTRALIA (email: a.vanschaik@westernsydney.edu.au). (Corresponding Author: Chetan Singh Thakur)

ing two coupled diffuser grids and more complex biological models [5]. The CSEM Neuchatel team demonstrated a device whose output conveys spatial contrast rather than temporal contrast [6], which is a combination of an event and a frame-based vision sensor. The team of Etienne-Cumming developed a temporal change threshold detection imager [7], which changes the typical active pixel sensor (APS) CMOS pixel to detect a quantized absolute change in illumination. The spatial contrast retina [8] produces outputs in the form of events and features on-chip calibration. A voltage-based dynamic vision sensor (DVS) converts the temporal contrast (TC) of the intensity of light into address events that are sent asynchronously for processing [10]. However, it does not implement explicit filtering and instead relies on non-linear filtering from parasitic capacitances in the front end.

In this work, we present a silicon retina model that closely emulates the functions and characteristics of the natural retina. Here, we adopted a current mode design approach to implement the required functions and filters, as these make it easy to implement some of the non-linear equations and the linear filters. The development of accurate and energy-efficient retinal circuits is important for advancements in retinal implants. Despite the existence of various artificial retinal implementations, the quest for a more realistic and precise model remains crucial. The motivation behind this work is to maximize information transmission or feature detection and processing by successfully incorporating essential features such as spatio-temporal band-pass filtering, luminance adaptation, contrast gain control, tonic cells, and phasic cells. We aim to enhance the sensory system's capacity to detect stimulus edges, maintain perceptual sensitivity in varying illumination conditions, optimize information transmission, and extract crucial visual features. The center-surround structure of the receptive field plays a vital role in promoting lateral inhibition, which improves the sensory system's capacity to detect the edges of stimuli. To maintain perceptual sensitivity in different illumination conditions, the temporal dynamics and gain of neural response must be adjusted through adaptations such as luminance and contrast gain control. Emulating the behavior of tonic and phasic cells is important to detect the presence of the visual stimulus and detect important features from it. Several studies have supported the importance of lateral inhibition, luminance adaptation, contrast gain control, tonic cells, and phasic cells [15]–[27]. The results of this study have the potential to drive significant advancements in computer vision, providing a solid foundation for the development of more efficient and reliable visual recognition systems.

To replicate these biological features in hardware, analog neuromorphic circuits can be the best option as supported by the previous studies [4], [28]–[32]. The low power consumption of neuromorphic circuits is attributed to their typical operation on the principle of collective computations and functioning within the weak inversion region of a transistor. However, the circuit dynamics of a biological retina necessitate relatively long time constants, which are difficult to achieve in semiconductor-based integrated circuits. Furthermore, analog circuits are not easily reconfigurable due to their reliance on the precise tuning of circuit parameters and their sensitivity to environmental factors, making it difficult to make changes without significant redesign. This restricts their versatility to perform different functions.

A novel bio-plausible spatio-temporal silicon retina is developed by employing neuromorphic analog VLSI circuits, with the simplified schematic representation depicted in Fig. 1. The design introduces novelties in both emulating biological features on the chip and the circuit design. The following elements are key contributions of this work:

- The analog silicon retina developed in this study features a non-separable center-surround filter that takes into account the natural delay of the surround signal transmission observed in real retinas. The outer plexiform layer (OPL) is spatially implemented as a difference of Gaussians (DoG) and a biphasic filter temporally. As a result, the spatio-temporal OPL filter can detect both edges and movements simultaneously.
- Unlike a separable filter, this center-surround filter is capable of detecting changes in luminosity even in a region where the luminosity is uniform.
- Luminance adaptation is represented using a high-pass filter.
- Contrast gain control properties of bipolar cells subject to shunting inhibition, are modeled as a leaky integrator with a leak conductance that is determined by the spatio-temporal neighborhood of contrast magnitude.
- This retina involves adaptable band-pass temporal filtering. Tonic cells and phasic cells are realized in this retina by changing the time constant associated with the high-pass filter.
- On the circuit side, a significant achievement is the development of a novel absolute value circuit to develop the contrast gain control mechanism between bipolar cells and amacrine cells.
- The analog silicon retina that has been proposed is capable of reconfiguration, offering a versatile platform to explore the visual operations of retinal circuits in a natural visual environment.

The remainder of this paper is structured as follows: Section II and III provide a description of the retina architecture and elaborate on the retinal pixel design. Results and discussion are presented in Section IV, and the article concludes with Section V.

II. Retina Architecture

The Convis retina model [33] serves as the basis for the silicon retina architecture, which includes all major types of neurons found in the layers of the biological retina, from photoreceptors to ganglion cells. The absorption of photons by photosensors is illustrated in the simplified schema of the retina model presented in Fig. 1a. The lateral inhibition is mediated by horizontal cells creating a center-surround receptive field. The photoreceptors and horizontal cells are collectively done by the OPL layer. The function of this OPL layer is to operate as an edge and a movement detector at the same time. It is implemented by using spatial filters, temporal high-pass, and low-pass filters. The output of the OPL layer is

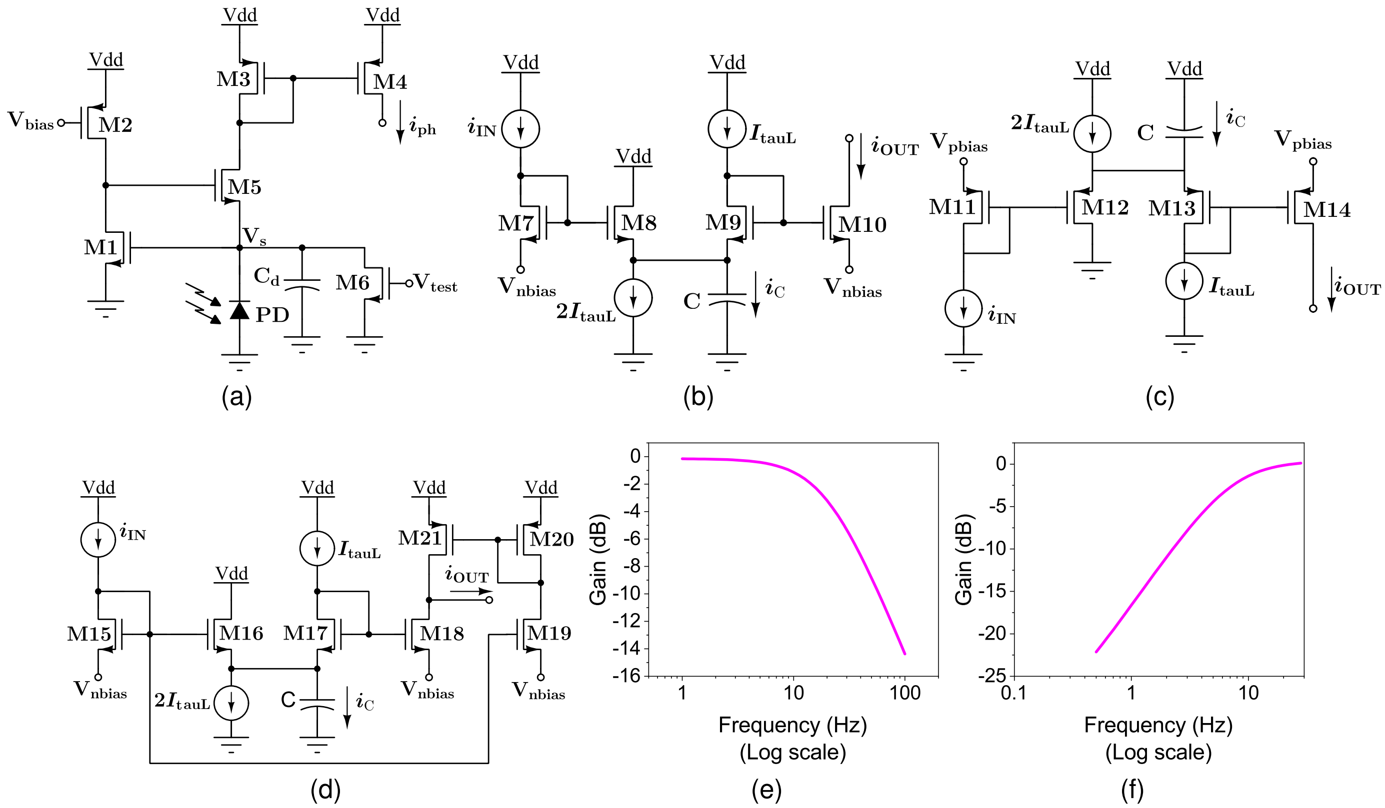

Fig. 2. (a) CMOS implementation of photocurrent transduction circuit consisting of photodiode (PD) and a feedback loop implemented by M1, M5 to increase the bandwidth as shown in [34]. (b) CMOS implementation of first-order log domain low-pass filter (tau-cell) as shown in [35] with N-Type MOSFETs models E_{C} and E_{S} of Eq. (1) and (2); (c) Similar implementation shown with P-Type MOSFETs models E_{A} from Eq. (14), Eq. (12) and (13); (d) CMOS implementation of first-order log domain high-pass filter (tau-cell) as shown in [36] implements T_{C} of Eq. (1); (e) Frequency response showing low pass characteristic of first-order log domain low-pass filter (tau-cell) as shown in Fig. 2b; (f) Frequency response showing high pass characteristics of first-order log domain high-pass filter (tau-cell) as shown in Fig. 2d.

a band-limited signal. This signal is fed into the contrast gain control stage for adapting different levels of light contrast. At the intersection of bipolar and amacrine cells, this gain control mechanism occurs through the utilization of a spatial filter, temporal low-pass filters, and a static activation function. The output of this stage is rectified before feeding it to the LIF neuron to generate spikes. The LIF neuron acts as a ganglion cell in the biological retina. Subsequent subsections provide a detailed description of each stage of the architecture.

A. *Outer Plexiform Layer (OPL)*

The OPL layer uses a collection of linear filters to transform the luminance input into two distinct signals: the center current I_{C}, and the surround current I_{S}. These two signals are subsequently subtracted from each other to produce the OPL current I_{OPL} [27], [33] as

$$I_{\mathrm{C}} = G_{\mathrm{C}} * T_{\mathrm{C}} * E_{\mathrm{C}} * L \tag{1}$$

$$I_{\mathrm{S}} = G_{\mathrm{S}} * E_{\mathrm{S}} * I_{\mathrm{C}} \tag{2}$$

$$I_{\mathrm{OPL}} = I_{\mathrm{C}} - I_{\mathrm{S}} \tag{3}$$

where L represents the luminance input, while G_{C} and G_{S} denote spatial (Gaussian) filters applied to the center and surround areas, respectively. Additionally, T_{C} denotes a high-pass filter, while E_{C} and E_{S} represent low-pass filters. The asterisk symbol (*) represents the convolution operation. The center signal and surround signal are associated with the activity of photoreceptors and horizontal cells in the biological retina. The current-mode analog circuit realization of the OPL elements is discussed below.

1) Luminance input (L): The circuit illustrated in Fig. 2a transforms collected photons into an electric current, resulting in the luminance input L. The transistor M1 is a common-source amplifier, and M5 is a feedback transistor (a source follower). The source follower detects photocurrent and establishes a feedback mechanism. As a result, the voltage across the photodiode is clamped to the output voltage of the common-source amplifier. The inclusion of this high-gain negative feedback loop that connects the source and gate of the current-sensing MOSFET in the source-follower configuration can lead to an improvement in the response speed of the photodiode [34]. The pMOS transistors M3 and M4 mirror the generated photocurrent. In the absence of the feedback transistor, the bandwidth provided by the photosensor is severely limited due to the diode junction capacitance and parasitic capacitance associated with the output node. These capacitances need to be charged or discharged by the very small photocurrent (in the order of pA). Because the current flowing through the capacitors (i.e., the photocurrent) is extremely small, the charging process of these capacitances takes a significant amount of time. Hence, there is a delay

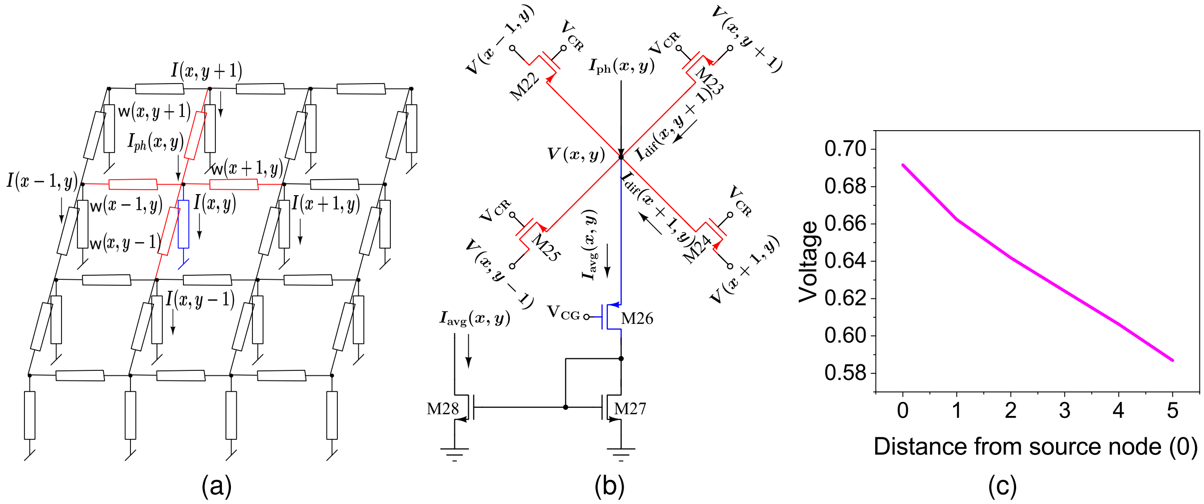

Fig. 3. (a) Depiction of two-dimensional diffusion network, implemented for spatial filtering in retinal layers (OPL and Bipolar layers) where each element in the horizontal surface (x-axis and y-axis where few elements are marked as red) represents resistance elements while the elements on the z-axis (one element shown in blue) represent conductance, where both the elements are implemented using MOS transistors; (b) CMOS implementation of a cell (marked in red and blue in Fig. 3a) builds spatial filtering operation as shown in [32] and the function of this circuit is to implement G_{C}, G_{S}, G_{A} as described in Eq. (1), (2), and (14); (c) Response of a signal($I_{\mathrm{ph}}(x, y)$) injected into the 2D diffusion network shown in Fig. 3a showing the decays with distance from the reference source node (0).

when we have a change in photocurrent due to the transient of this photocurrent mirroring stage, which thus has a low-pass-filtering effect on the photocurrent.

2) Temporal low-pass filter (E): The Log domain circuit design approach is employed to create the temporal low-pass filter in current-mode analog circuits [37]–[39]. It is the easiest and most efficient way to describe the first-order differential equation for a filter. The circuit diagram of the temporal low-pass filter (nMOS-and pMOS-based) is depicted in Fig. 2b and 2c. The transistors in the circuit are operating in the weak inversion region. This circuit, also known as tau-cell, is built around the translinear loop as defined in the below equation as

$$i_{\mathrm{IN}} \cdot I_{\mathrm{tauL}} = (I_{\mathrm{tauL}} + i_{\mathrm{C}}) \cdot i_{\mathrm{OUT}} \tag{4}$$

The loop comprises two current sources, I_{tauL} and $2I_{\mathrm{tauL}}$, as well as a capacitor. Because the current source I_{tauL} supplies a constant current, V_{gs9} remains constant in Fig. 2b, and hence, changes in capacitor voltage appear as changes in V_{g9}. This circuit includes programmable DC gain, which may be increased or decreased by changing the currents I_{tauL} or $2I_{\mathrm{tauL}}$. Voltage sources $\mathrm{V_{nbias}}$ and $\mathrm{V_{pbias}}$ are used in place of common grounds in nMOS and pMOS tau-cell filters depicted in Fig. 2. In Fig. 2b, if the source terminal of M7 is connected to the ground and both M7 and M8 carry the same currents, then the source terminal of M8 is also ground. But the source terminal of M8 is attached to a current source carrying the current $2I_{\mathrm{tauL}}$. If the current source is implemented using a MOS transistor, then the potential of both the drain and source is zero. In order to avoid the source of M8 going to zero potential, $\mathrm{V_{nbias}}$ is used in Fig. 2b. The time constant of the filter in this circuit is independent of the input signal, which is a significant advantage. The equation describes the relationship between the input and output currents as given by,

$$\tau_l \frac{di_{\mathrm{OUT}}}{dt} + i_{\mathrm{OUT}} = i_{\mathrm{IN}} \tag{5}$$

$$\tau_l = \frac{C}{gm9}$$

where τ_l is the time constant and the transconductance $gm9$ is determined by I_{tauL}, the current through the transistor M9. This first-order linear differential equation implies that the above circuit operates as a current domain first-order low-pass filter. The time constant remains constant regardless of input current change, and it is regulated by the external bias current I_{tauL}. These filters can achieve long-time constants similar to those of the biological retina. Retinal processing involves low-pass filtering, which begins at the photoreceptor level with the complex phototransduction cascade and continues in subsequent layers due to synaptic delays and the integration of synaptic currents by the cell membranes. The frequency response of the tau-cell low-pass filter is depicted in Fig. 2e. The cut-off frequency is chosen based on the biological time constant as in the software model.

3) A temporal high-pass filter (T): The interaction between inhibitory and excitatory cells within various layers of the biological retina produces high-pass filtering behavior, as explained in [40]. Inhibitory cells such as horizontal cells in the outer plexiform layer (OPL) and amacrine cells in the inner plexiform layer (IPL) contribute to this effect. The high-pass response observed in a biological retina is influenced by various control loops, including those related to photo-transduction, synaptic receptor desensitization, as well as fast and slow gain adaptation. Short-term luminescence adaptation of photoreceptor cells is captured by the high-pass filter [33]. The analog retina circuit can replicate the functioning of tonic and phasic cells that are present in the biological retina by

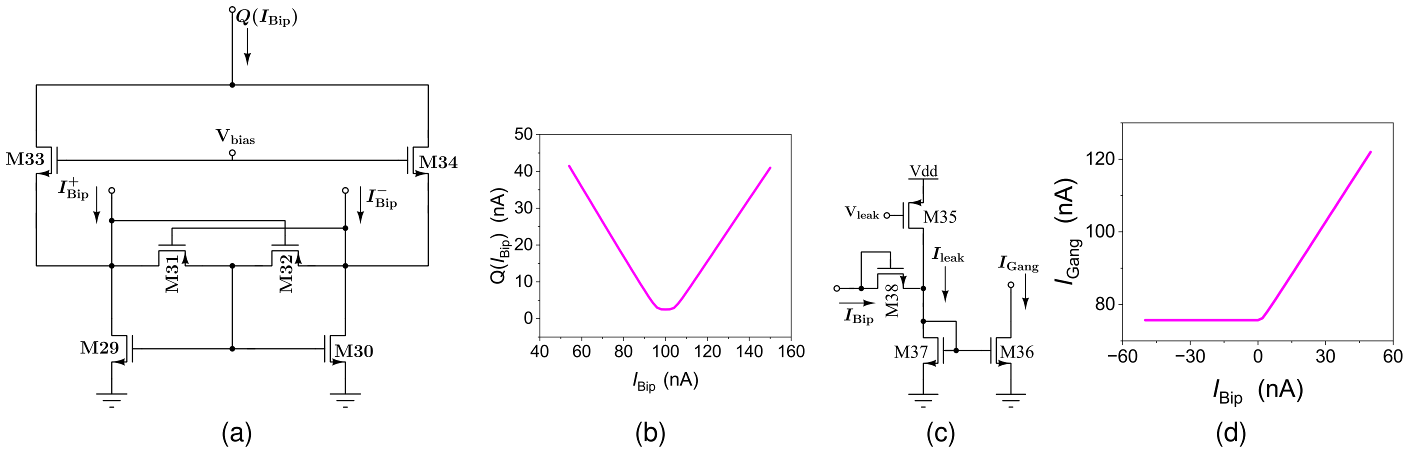

Fig. 4. (a) CMOS implementation of a novel absolute-value circuit modeling the activation function $Q(I_{\text{Bip}})$ of the bipolar layer's contrast gain control mechanism; (b) Characteristic response of the absolute-value circuit shown in Fig. 4a showing an approximation of static activation function $Q(I_{\text{Bip}})$; (c) CMOS current mode implementation of static nonlinearity function $N(I_{\text{Bip}})$; (d) Static nonlinearity function generated using the circuit shown in Fig. 4c to rectify signal I_{Bip} before feeding it to ganglion cells for spike generation.

modifying the time constant of the high-pass filter [40]. Tonic or sustained cells have a low activation threshold and respond continuously to a stimulus for as long as it is present, making them highly sensitive to low-contrast stimuli. Transient or phasic cells, on the other hand, have a high activation threshold and respond briefly to a stimulus before quickly adapting. They are particularly sensitive to high-contrast stimuli [27].

In the low-pass filter circuit shown in Fig. 2b, the weight, which is represented by the current I_{tauL} acts as a scaling factor that controls the strength of the filter. By varying the current, we can adjust the amount of high-frequency components that are removed from the signal. The log domain high-pass filter circuit is shown in Fig. 2d. It is implemented by using a tau-cell low-pass filter, subtracting the tau-cell low-pass filter output from the original input signal. The input signal flows through transistors M15 and M19, while the low-pass filter output is obtained at transistor M18. The high-pass filter current I_{out} flows out as the difference between the original input current and the current from the tau-cell low-pass filter. The transfer function of the high-pass filter circuit is defined by,

$$T_\omega = \frac{s\tau_h}{s\tau_h + 1} \tag{6}$$

where τ_h is the time constant of the high-pass filter circuit.

4) Spatial low-pass filters (G): Spatial filtering refers to the filtering methods that are performed directly on the pixels. The sum of products of the mask coefficients or weights with the corresponding pixels right under the mask is all that is required. In the biological retina, spatial low-pass filtering encompasses electrical coupling through neighboring cells and synaptic integration of dendrites of retina cells. Mathematically, these biological processes can be viewed as spatial averaging of the input signal. If $I(x, y)$ is the pixel intensity at position (x, y), then the sum of products of all neighboring pixels connected to $I(x, y)$, as well as the corresponding weights of all edges, are described as

$$\begin{aligned} I(x,y) = \mathrm{w}(x-1,y) * I(x-1,y) + \mathrm{w}(x+1,y) * \\ I(x+1,y) + \mathrm{w}(x,y-1) * I(x,y-1) \\ + \mathrm{w}(x,y+1) * I(x,y+1) \end{aligned} \tag{7}$$

This procedure applies to every pixel in an image. The diffusion network, shown in Fig. 3a, computes Eq. (7) and is employed in the construction of such a filtering process [41]–[43], [44].

Current injected at a node in the diffusion network diffuses laterally and decays at a distance defined by the diffusion length L [32],

$$L = 1/\sqrt{RG} \tag{8}$$

where R is horizontal resistance, and G is vertical grounded conductance. Since the network is linear, the effects of currents injected at different nodes superimpose in the resistive grid, where resistance values correspond to the weights of the equation. Since controlling diffusion length is challenging, transistors that operate in the subthreshold region are used to replace the resistors. This is illustrated in Fig. 3b.

Resistance or conductance between the nodes can be changed by varying the transistor gate-to-source voltage. In other words, the current between the drain and source terminals I_{ds} is used to define the weights. The equation for I_{ds} is written as,

$$I_{\text{ds}} = I_{\text{o}} exp(\frac{V_{\text{gs}}}{\eta U_{\text{T}}}), \qquad (V_{ds} > 4U_T) \tag{9}$$

where, I_{o} represents the residual saturation drain current, η denotes the slope factor, and U_{T} represents the thermal voltage. Since the transistors are operating in a weak inversion region, the diffusion length can be rewritten as [45]

$$L = exp(\frac{V_{\text{CR}} - V_{\text{CG}}}{2\eta U_{\text{T}}}) \tag{10}$$

$$= \sqrt{\frac{I_{\text{CR}}}{I_{\text{CG}}}} \tag{11}$$

where I_{CR} and I_{CG} are control currents proportional to V_{CR} and V_{CG}.

Gap junctions connect photoreceptors to each other in the outer plexiform layer, and a spatial filter is employed to incorporate the spatial blurring caused by these junctions. Horizontal cells are closely interconnected through gap junctions and synaptic pooling. They have larger receptive fields and are specialized for pooling and processing visual information over larger spatial scales. The larger receptive field and low-pass nature of horizontal cells mean that they need to use a spatial filter with a larger sigma value (standard deviation of a 2D Gaussian function) to effectively capture and process the visual information over these larger scales. In contrast, photoreceptors, with their smaller receptive fields, do not need such a large sigma value in their spatial filter as they are better suited to detect fine details in the visual scene. In the biological retina, horizontal cells receive signals from photoreceptors with a delay. This delay is emulated using a temporal low-pass filter. Even while the delay between the center and surround signals is small, barely a few milliseconds in mammalian retinas, it has major perceptual repercussions [40]. Due to the delay in transmitting the surround signal, the center-surround OPL filter can detect temporal changes in brightness, even in areas that have uniform spatial characteristics. The exponential filters and the difference of Gaussians (DoG) are used to generate the OPL layer as shown in Eqs. (1-3).

B. Contrast Gain Control Mechanism in Bipolar Cells

The visual system must cope with a wide range of light levels, spanning about 14 orders of magnitude [46]. Photoreceptors cannot cover such a range, hence our eyes need to adapt to sudden changes in light levels. To address this issue, the visual system employs multiple stages of gain control, including iris constriction, photoreceptor adaptation, and cortical lateral inhibition [47], [48]. The gain control between bipolar cells and amacrine cells in the retina is referred to as contrast gain control, whereby the output gain is controlled by the input contrast. Experimental evidence demonstrated this by presenting different contrast stimuli across the receptive field of the cell and evaluating the input-output relationship.

The equation that models the mechanism of contrast gain control [27], [33] is mentioned in the following text. It is a non-linear feedback loop that adapts the gain according to local contrast. Modeling the contrast gain control properties of bipolar cells subject to shunting inhibition involves a leaky integrator with leak conductance that depends on a spatio-temporal neighborhood of contrast magnitude as given by,

$$I^{+}_{\text{Bip}} = C\frac{dV^{+}_{\text{Bip}}}{dt} = I_{\text{C}} - g_{\text{A}}V^{+}_{\text{Bip}} \tag{12}$$

Here, the center signal I_{C} from the OPL layer is gain-controlled by bipolar-amacrine synapses modeled as a leaky integrator. Similarly, the surround signal I_{S} is gain-controlled by the equation as

$$I^{-}_{\text{Bip}} = C\frac{dV^{-}_{\text{Bip}}}{dt} = I_{\text{S}} - g_{\text{A}}V^{-}_{\text{Bip}} \tag{13}$$

The process of generating the gain-controlled currents I^{+}_{Bip} and I^{-}_{Bip} are regulated by a feedback mechanism in bipolar cells. This feedback loop adjusts the sensitivity of the visual system to local contrast by integrating linear current I_{C} and I_{S} into the bipolar cell with potential V^{+}_{Bip} and V^{-}_{Bip}. This feedback is provided by the leak conductance g_{A} as

$$g_{\text{A}} = G_{\text{A}} * E_{\text{A}} * Q(I_{\text{Bip}}) \tag{14}$$

Since the leakage determines the gain of current integration, g_{A} has a divisive effect. At the same time, g_{A} defines the time constant of Eq. (12) and (13). g_{A} is not the instantaneous input from a single pixel, it is a spatially (G_{A}) and temporally (E_{A}) smoothed version of the neighboring pixels and g_{A} can vary based on the static activation function Q.

$$Q(I_{\text{Bip}}) = g^{0}_{\text{A}} + \lambda_{\text{A}}(I^{+}_{\text{Bip}} \cdot I^{-}_{\text{Bip}}) \tag{15}$$

The Q function is the non-linearity that characterizes the gain control behavior employed in the software model [33]. Q is assumed to have a parabolic shape, implying different behaviors of the system, depending on the contrast. In high contrast, Q enters into a high-value range, and the leakage of the integrators shown in Eq. (12) and (13) is large. In small contrast, the values of Q are small and the leakage of the integrators is small. This way a cell is automatically adapted to the contrast of the neighboring pixels. The contrast of neighboring cells affects how a cell will respond to its input. In Eq. (15), the variable g^{0}_{A} corresponds to the inert leaks in the membrane integration process. Conversely, λ_{A}, also present in Eq. (15), determines the magnitude of the gain control feedback loop. This Q function is approximated by the absolute value circuit which has the response of a full-wave rectifier as shown in Fig. 4b.

We have designed a novel absolute value circuit to model the Q function using current-mode circuits, as depicted in Fig. 4a. In this circuit, the input currents are I^{+}_{Bip} and I^{-}_{Bip}, and the output current is $Q(I_{\text{Bip}})$. The voltage at the drain node of M30 is small when the current $I^{+}_{\text{Bip}} > I^{-}_{\text{Bip}}$. When the node voltage is sufficiently small to turn the pMOS transistor M31 ON, the diode-connected loop forms around the transistor M29. The current I^{+}_{Bip} flows through M29, and it generates corresponding voltage V_{gs} across the gate and source of M29. Note that V_{gs} of M29 is shared with the gate and source of M30, and the current I^{+}_{Bip} should flow through M30 as well. Since the current I^{-}_{Bip} is sufficiently small, the transistor M30 pulls the current through M34. The transistors M29 and M30 now operate as a current mirror. When the current I^{+}_{Bip} is increased, the current through M30 increases linearly via M34.

$$I_{34} = \frac{(W30/L30)}{(W29/L29)} I^{+}_{\text{Bip}} \tag{16}$$

If $I^{+}_{\text{Bip}} < I^{-}_{\text{Bip}}$, the circuit operates in the same manner as in the previous case and current through M33 is now increasing linearly as I^{-}_{Bip} - I^{+}_{Bip} grows.

$$I_{33} = \frac{(W29/L29)}{(W30/L30)} I^{-}_{\text{Bip}} \tag{17}$$

At the output node

$$Q(I_{\text{Bip}}) = I_{33} + I_{34} \tag{18}$$

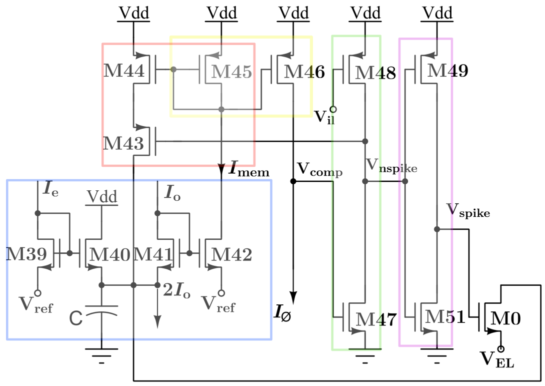

(a)

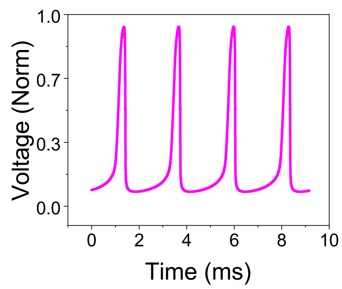

(b)

Fig. 5. (a) Shows CMOS implementation of Mihalas-Niebur neuron model mimicking ganglion cell of the biological retina as shown in [51]; (b) Depicts the output spikes of Mihalas-Niebur neuron.

Hence, full wave-rectified response can be observed at $Q(I_{\text{Bip}})$. The approximation in Eq. (18) is intended to capture the essence of the nonlinearity described in Eq. (15) using a simpler, circuit-friendly representation.

The gain-controlled center and surround currents are subtracted and passed as a single signal from the bipolar layer,

$$I_{\text{Bip}} = I^{+}_{\text{Bip}} - I^{-}_{\text{Bip}} \tag{19}$$

C. Inner Plexiform Layer (IPL) and Ganglion Cells

The second layer of synapses in the retina is represented by the inner plexiform layer (IPL), where bipolar cells, amacrine cells, and ganglion cells interact through synaptic connections. Previous research [47], [49], [50], suggests that the IPL plays a role in contrast gain control. The section below outlines the process of converting the bipolar cell current (I_{Bip}) into an excitatory current (I_{Gang}), which is then used to trigger output spikes in a leaky integrate-and-fire neuron.

1) Synaptic current upon ganglion cells: The formula to simulate the signal transformation from bipolar cells to ganglion cells is given by,

$$I_{\text{Gang}} = N(I_{\text{Bip}}) \tag{20}$$

where I_{Gang} is the excitatory current on ganglion cells. I_{Bip} is the bipolar layer output current and $N(I_{\text{Bip}})$ is the static non-linearity function upon I_{Bip}. I_{leak} is the leak of the static non-linearity function. In this function, the negative data are chopped off. Saturations and synaptic transmissions are some causes behind the static non-linearities of the biological retina.

The circuit implementation of the static non-linearity function is shown in Fig. 4c, and it is formed by the diode-connected transistors M37 and M38, as well as M35 and M36. The diode-connected transistor M38 removes any negative samples of the bipolar output. The half-wave rectification function is performed by the diode-connected transistors M37 and M38. The transistor M35 exhibits a leakage function, with a value beyond which the transmission transitions to a linear state. The response of the circuit implementation of the static non-linearity function is as shown in Fig. 4d. The equation for the current I_{Gang} from the circuit is written as

$$I_{\text{Gang}} = \frac{(W36/L36)}{(W37/L37)}[I_{\text{Bip}} + I_{\text{leak}}] \tag{21}$$

2) Ganglion layer: Non-spiking neurons do most calculations in the biological retina up to this point. However, the biological retina output is spike train and contains information about the scene. Ganglion cells are responsible for generating spikes in the actual retina, and LIF neurons are used to mimic them in this retina implementation. The conversion of the signal I_{Gang} that varies continuously over time, into discrete sets of single spikes is achieved through the use of the following formula as

$$\frac{dV_n}{dt} = I_{\text{Gang}} - g_L V_n \tag{22}$$

where the cell potential is denoted by V_n, and the time constant is represented by g_L. When a neuron is in its refractory period, V_n remains constant at 0. Once V_n surpasses a specific limit, it is then reset to 0. Mihalas–Niebur neuron is used for the spiking activity in this analog retina that comprises a tau-cell to model leaky integrate-and-fire functionality of the real neuron [51]. Mihalas-Niebur neuron model is implemented using log-domain current-mode circuits [51], [53], as shown in Fig. 5. To represent the leaky integration of a neuron, a first-order low-pass filter configured as a tau-cell is employed. This tau-cell is enclosed within a blue box and formed by transistors M39 to M42. The filter creates a current I_{mem} at its output. To generate a spike, I_{mem} is copied by using the current mirror transistors M45 and M46 (yellow box). It is compared using the constant threshold current I_{ϕ}. Because I_{mem} can be approximately close to I_{ϕ}, a current-limited inverter, comprised of transistors M47 and M48 and enclosed in a green box, is incorporated to bring down power consumption. This inverter generates a digital value V_{nspike}, and it results from a comparison between I_{mem} and I_{ϕ}. The second inverter pair (purple box) formed by M49 and M51 to generate a positive voltage spike V_{spike} with a slight delay regarding V_{nspike}. As indicated in the orange box, positive feedback is implemented by employing PMOS transistors M45, M44, and M43, with the feedback relying on V_{nspike}. The transistor M0 is used to reset the membrane current to a particular value, and this value is regulated by V_{EL}.

III. Pixel Circuit

The pixel circuit is implemented based on the retinal equations discussed in Section II. The silicon retina comprises

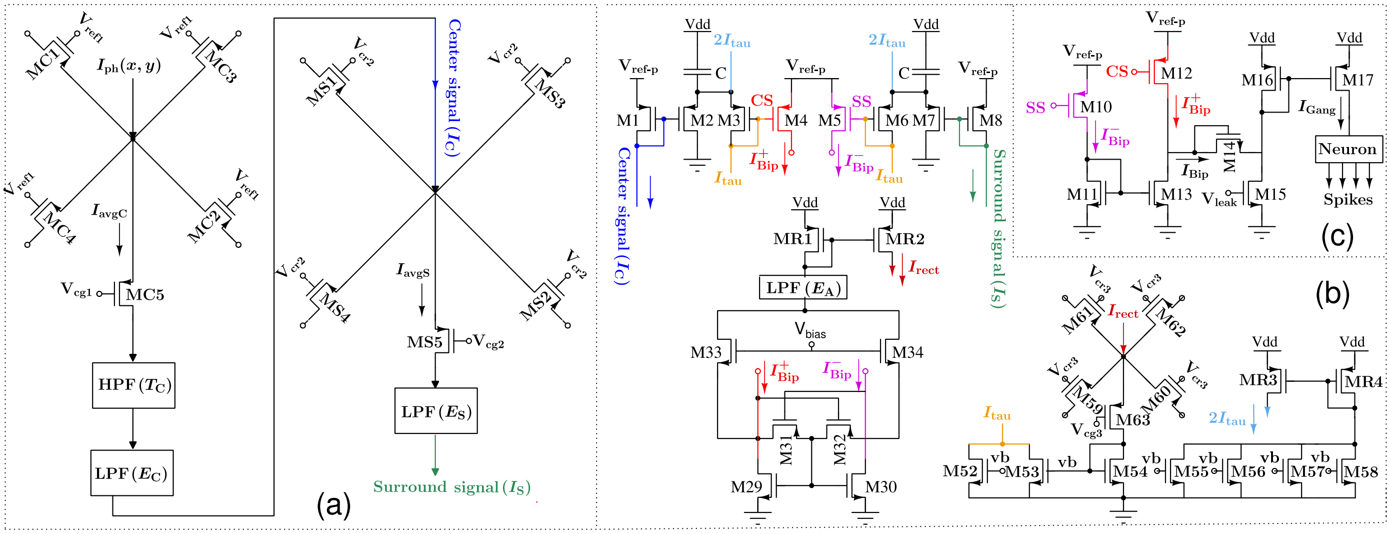

Fig. 6. CMOS implementation of (a) outer plexiform layer (OPL) layer with ($I_{\text{ph}}(x, y)$) to photoreceptor cells as the input and center signal, surround signal as the corresponding outputs; (b) Bipolar layer with contrast gain control accepting center signal and surround signal as input from OPL layer and I^+_{Bip}, I^-_{Bip} as gain controlled outputs; (c) Static activation function passed as input to neuron model implemented in Fig. 5 generating spiking outputs.

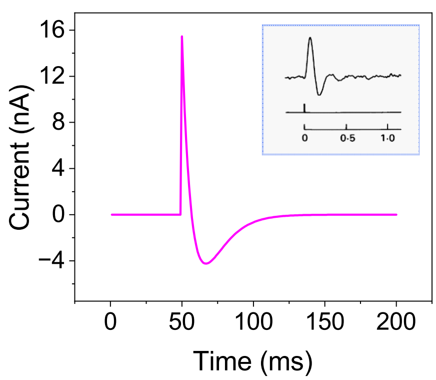

Fig. 7. The impulse response of the center component (photoreceptor cell) shown in Fig. 6a for a given impulse input (I_{ph}) to the photoreceptor cell. This response is close to that is seen by Schnapf [52] in the photoreceptor cell of the macaque monkey and it is shown inside the blue box.

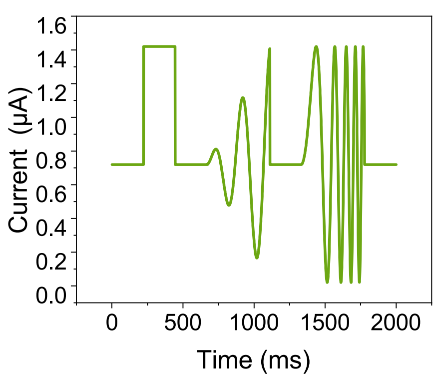

Fig. 8. A sample "chirp" test stimulus is passed as input (I_{ph}) to the pixel circuit shown in Fig. 6a.

several pixel arrays, and each pixel models the complete set of retina equations. The circuits discussed in section II are the building blocks of each pixel circuit. The pixel circuit is depicted in Fig. 6, and each pixel of the pixel array is connected to its neighbors to perform spatial filtering. Incoming light intensity is converted to electrical current using the photosensor circuit shown in Fig. 2a. This equivalent current of the light intensity is injected into the spatial filtering circuit of the center component. This spatially-smoothed signal is applied as the input of two series-connected filters, a high-pass filter (T_C), and a low-pass filter (E_C), as depicted in Fig. 6a. The signal at this point is called the center signal. This signal is further smoothed spatially by a spatial filter with a big sigma value, and another low-pass filter (E_S) delays it to generate the surround signal.

The contrast gain control circuit in Fig. 6b receives input from the OPL stage. Both the center signal (I_C) and surround signal (I_S) are applied as input to two separate pMOS tau-cell log domain low-pass filters. The tau-cell filter output for the center signal is represented by the drain current of M4, and the drain current of M5 is the filter output corresponding to the surround signal.

These two filtered currents are designated as I^+_{Bip} and I^-_{Bip}, respectively. Currents I^+_{Bip} and I^-_{Bip} are flowing through the absolute value circuit formed by transistors M29-M34. The rectified current of the absolute value circuit is then temporally and spatially-smoothed by the temporal low-pass (E_A) and spatial low-pass filters. The filtered output current of the spatial filter represents g_A of the Eq. (14). Spatially filtered current I_{tau} adjusts the time constant of both the pMOS tau-cell filters. This is how the contrast gain control circuit works in different input contrast. The gain-controlled currents I^+_{Bip} and I^-_{Bip} are subtracted at the output of M12 and M13 as shown in Fig. 6c, and the resultant current then passes through the transistors M14-M17 which implements $N(I_{\text{Bip}})$ function as depicted in Fig. 4d. The current I_{Gang} obtained at the drain of M17 is the input to the LIF neuron that generates spikes.

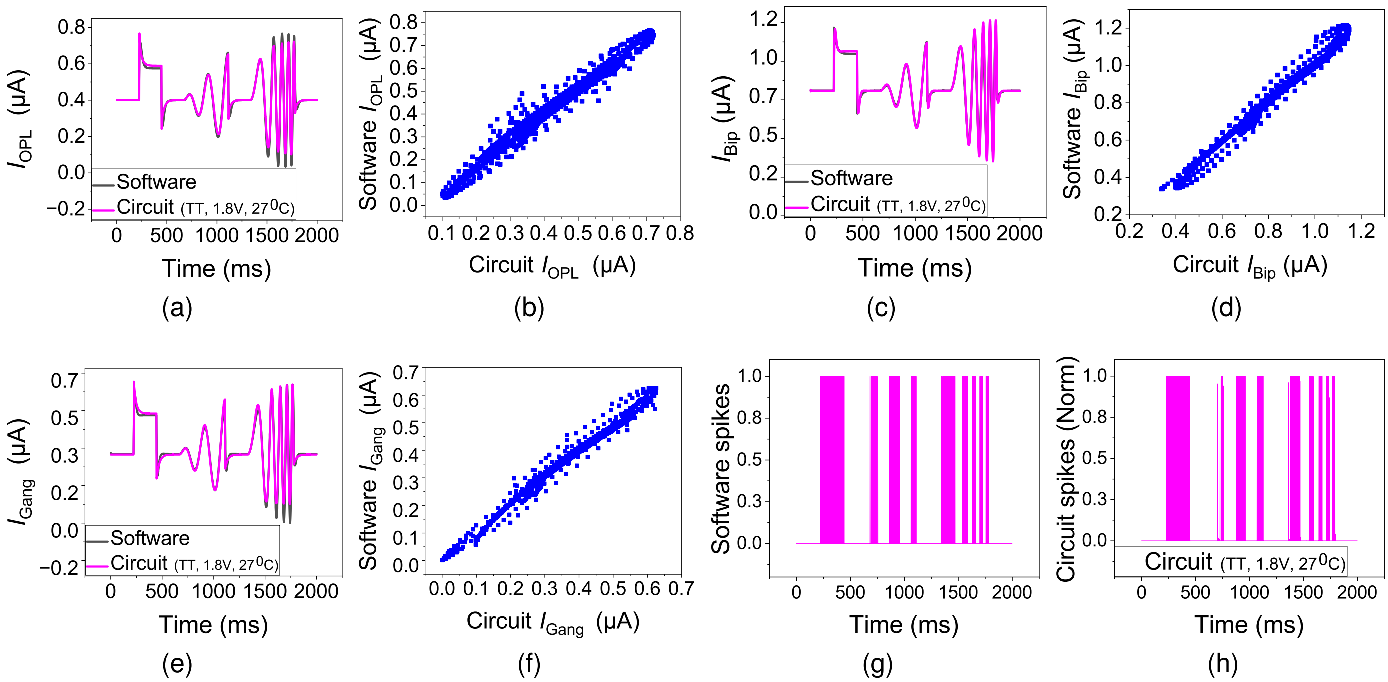

Fig. 9. A comparison is made between the stages of the software retina model (Convis) and the analog retina circuit, utilizing a chirp stimulus input depicted in Fig. 8. Specifically, (a) shows the OPL current I_{OPL}, while (b) compares the software retina OPL current trace to that of the retina circuit. Likewise, (c) shows the bipolar current I_{Bip}, and (d) compares the software retina bipolar current trace to the retina circuit. Additionally, (e) displays the excitatory current on ganglion cells I_{Gang}, and (f) compares the trace of this current to that of the retina circuit. Fig. 9 also illustrates the responses of the software spike generation in (g) and the circuit spike generation in (h).

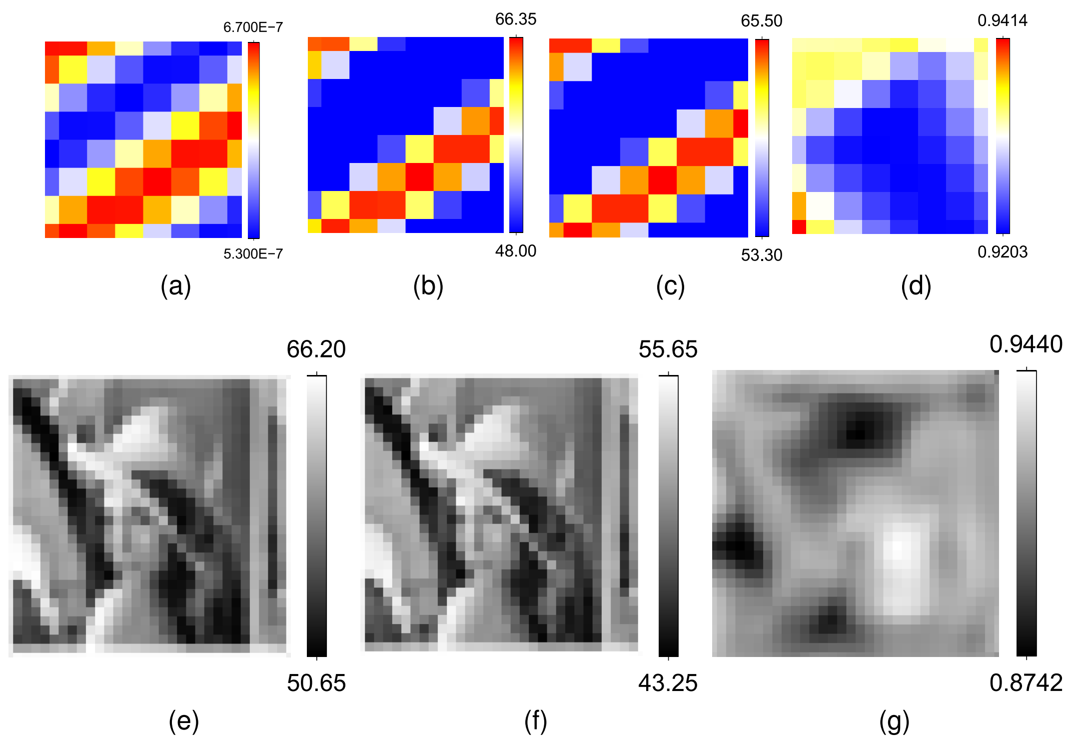

Fig. 10. Response showing structural similarity index measure (SSIM) to the sinusoidal grating stimulus (8×8) applied to both the photoreceptor cell in the analog retina pixel array and the software model where (a) Depicts the moving grating stimulus; (b) Illustrates the output current of the ganglion cells (I_{Gang}) for the software model (shown in nA scale); (c) Shows the analog circuit current response of the ganglion cells (I_{Gang} shown in nA scale); (d) Shows the local SSIM map with global SSIM value=0.93; Response of the retina to a (32×32) image where (e) Shows the ganglion current I_{Gang} response to the applied image into the software; (f) Shows the analog retina response of ganglion current I_{Gang} (shown in nA scale); (g) Shows the local SSIM map with global SSIM value=0.91.

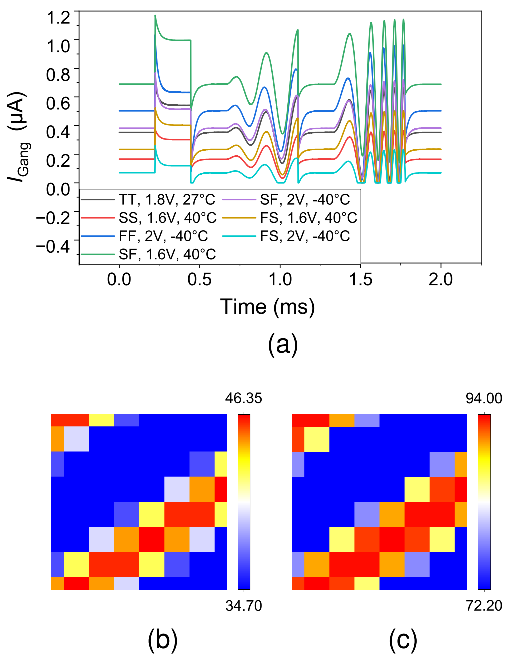

Fig. 11. (a) PVT analysis is conducted on an 8×8 analog retina pixel array, and the current I_{Gang}, associated with a pixel for the chirp stimulus shown in Fig. 8, is graphed for the TT, SS, FF, SF, and FS process corners. The supply voltage ranges between 1.6V and 2V, while the temperature spans from -40°C to 40°C. (b) Shows the SS corner I_{Gang} current response of the ganglion cells (shown in nA scale) for the given 8×8 grating stimulus; (c) Shows the FF corner I_{Gang} current response of the ganglion cells for the same 8×8 grating stimulus.

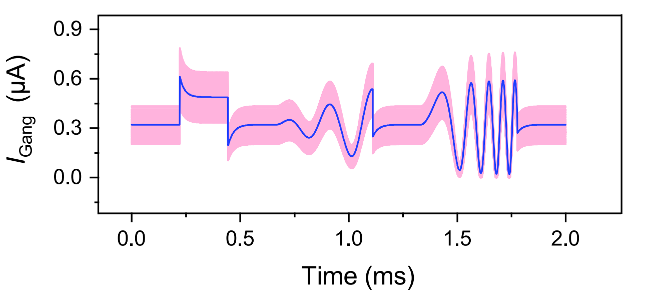

Fig. 12. Monte Carlo analysis is performed on the 8×8 retina pixel array, producing a plot that corresponds to the I_{Gang} current of a pixel for the chirp stimulus shown in Fig. 8. In this plot, the shaded region is indicative of variance, with the blue waveform depicting the mean. The Monte Carlo analysis involves selecting 200 iterations, utilizing a low-discrepancy sequence as the sampling method, applying the TT process corner under a temperature of 27°C, and the supply voltage is 1.8V.

IV. Results and Discussion

The response of the center-surround OPL filter to an impulse input, as illustrated in Fig. 7, bears a striking resemblance to the one quantified by Schnapf [52] in the retina of the macaque monkey. To ensure that the analog retina circuit matches the software retina model (Convis) [33], various stimuli and retina configurations are compared. To establish the properties of retinal ganglion cells and confirm that the temporal responses obtained from the circuit simulation align with those obtained from the software model, a chirp stimulus (shown in Fig. 8) is used. At the start of the chirp stimulus, there is a pulse that initially decreases, then increases, and then decreases in activity. This is followed by oscillations that grow in both frequency

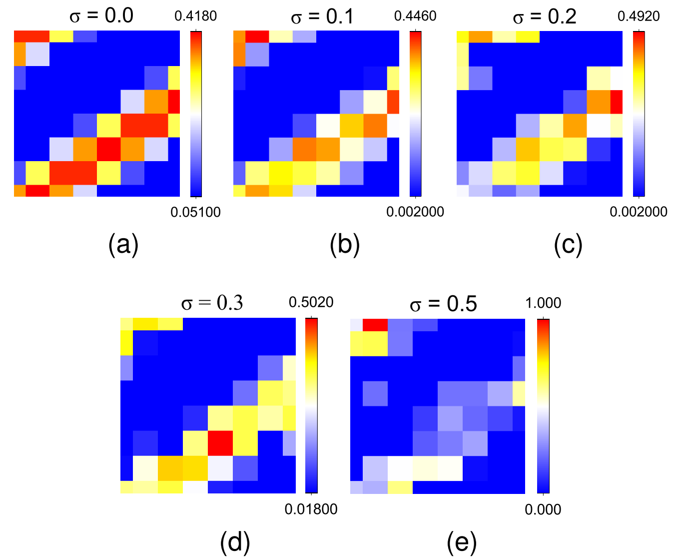

Fig. 13. Illustration of the impact of noisy images on the output of the retina pixel array, with a varying standard deviation (σ) of the noise. The normalized I_{Gang} output is shown in (a) in the absence of noise and (b)-(e) with a noise standard deviation of 0.1, 0.2, 0.3 and 0.5, added to the sinusoidal grating stimulus (8×8).

and amplitude, as described in [54]. Identical parameters are used in both circuit simulation and software simulation. The temporal comparisons of OPL, bipolar, and ganglion input layers are shown in Fig. 9. These figures demonstrate that the responses of the analog retina closely match those of the software retina. In Fig. 9, the simulation results are presented for a comparison of different architectures. The OPL layer shows a variance fraction of 94.8%, while the bipolar layer and the ganglion current demonstrate variance fractions of 95.96% and 94.93%, respectively. These results indicate that the output of the models is sufficiently similar that any differences become imperceptible when generating spikes.

A spatial comparison between the analog retina array and the software retina can be accomplished by employing a sinusoidal grating stimulus, as illustrated in Fig. 10a. The grating stimulus of size 8×8 is applied as the input to the 8×8 retina pixel array, and the corresponding I_{Gang} currents of the array are recorded. The images generated from the recorded outputs are compared against the software retina model using similarity index measure (SSIM). The SSIM map [55] is shown in Fig. 10d, along with the global SSIM value. This is a metric for comparing two images spatially. In the local SSIM map, small values of local SSIM appear as blue pixels. Areas where the analog retina output image considerably differs from the software output image correlate to regions with small local SSIM values. Bright red pixels arise when the local SSIM value is high. Large local SSIM regions correlate to uniform portions of the software image, where blurring has a lesser impact. The obtained SSIM value is 0.93. If the SSIM value is close to 1 indicating that both images are similar [55]. A Lena image of size 32×32 is applied as the input to the analog pixel array (32×32) and the software retina model. The I_{Gang} current resulting from this input is then plotted, as shown in

Fig. 10e and 10f.

A. Performance Analysis

This section shows the performance analysis of the retina pixel array (8×8) at 0.18μm technology node. Process, voltage, temperature (PVT) analysis, Monte Carlo analysis, and noise analysis are reported in this section.

1) PVT Analysis: Fig. 11a presents an analysis of the impact of supply voltage and temperature variation across five process corners. The MOS transistor corners were typical-typical (TT), slow-slow (SS), fast-fast (FF), slow-fast (SF), and fast-slow (FS). The analysis was conducted on an 8×8 analog retina pixel array, specifically centering on the current designated as I_{Gang}, which is associated with the response of an individual pixel to the chirp stimulus depicted in Fig. 8. This analysis covered a range of supply voltage between 1.6V and 2V, and temperature variations from -40°C to 40°C were considered.

2) Monte Carlo Analysis: To verify the robustness of the design against process and mismatch variations, a Monte-Carl (MC) analysis is conducted with 200 runs performed on the 8x8 retina pixel array. The analysis utilizes a low-discrepancy sequence sampling method and considers the process corner as TT at a temperature of 27°C. The resulting plot corresponds to a pixel is shown in Fig. 12. The shaded region on the plot indicates variance, while the blue waveform represents the mean.

Fig. 11a shows clear distinctions between the plots of process corners. To verify that the variations are within an acceptable range, we applied the 8×8 grating stimulus to the pixel array and plotted the I_{Gang} current at process corners SS and FF as shown in Fig. 11b and 11c. These resulting images exhibit visual similarities to the desired output displayed in Fig. 10c, and their edges are distinguishable.

3) Noise Analysis: This analysis explores how the retina responds to a simple visual stimulus (the sinusoidal grating) under different levels of noise as shown in Fig. 13. The standard deviation (σ) values represent the intensity or magnitude of noise added to the stimulus, simulating various levels of noise interference that the retina might encounter in real-world scenarios. In practical terms, it could represent various sources of noise that affect the visual signal, including environmental factors like random light fluctuations. As light is made up of a large number of photons, light fluctuations can be modeled as Gaussian noise. To model different scales of noise we vary the σ of Gaussian noise. Lower values of σ imply cleaner visual input, while higher values of σ indicate increased interference, potentially making it harder for the visual system to extract meaningful information.

Noise introduced by the circuit itself can negatively affect the performance of a silicon retina by reducing its accuracy, resolution, and reliability. In this silicon retina, the filters implemented in the OPL stage can minimize the noise produced by the circuits operating within the same OPL stage. Furthermore, in the later stage, the operation carried out at Eq. (19) can further reduce the noise that propagates through the subsequent stages of the silicon retina.

B. Measurement Results

A standard CMOS 0.18μm process technology from TSMC was used to fabricate the single pixel of the retina, as depicted in the die microphotograph shown in Fig. 14a. To evaluate the functionality of the pixel circuit, a test measurement setup was utilized, as illustrated in Fig. 14b. A custom IC test board was used to mount the test chip, and an interface built using Python programming language was employed to regulate the inputs and outputs. The test chip was directly linked to a high-precision analog testing equipment, which was operated through the interface. The required currents to the chip are supplied by current source equipment (Keithley 6221) and the capacitors in the chip are implemented by using MOSCap. Fig. 15 shows the measured result of the ganglion current I_{Gang} for the same chirp stimulus. Fig. 15 is plotted for the two values of the high-pass filter biasing current I_{tauh}. The result nearly resembles the intended desired shape and magnitude of the software output, as evidenced by the observation. The ratio of variance obtained for the measured response in comparison simulation with the software retina is 87.7%. To ascertain the amount of delay present in the measured signal, the technique of cross-correlating two signals is employed as stated in [56]. By performing this procedure, a peak is generated that represents the delay between the two signals. As illustrated in Fig. 15c, the peak is located at 0 steps, indicating that there is no time difference between the software and the measured output.

To validate the spatial filtering operation, it is necessary to place a pixel array on the chip. In this context, we initiated a comparative analysis between the circuit simulation results of the analog pixel array and the software retina array. We believe that if we measure a single pixel and it matches the corresponding pixel in the software-based retina, then when we put the pixel array on the chip, it should work properly. By comparing the simulation results of the analog pixel array with the software retina array, we can establish a correlation between the behavior of individual pixels. If the measured pixel aligns with the corresponding software retina pixel, it provides evidence that the pixel array, when implemented on the chip, is expected to exhibit similar functionality. This validation process helps to ensure the feasibility and effectiveness of using the analog pixel array on the chip for spatial filtering operations. However, while matching single-pixel measurements to simulations is a positive indicator, it doesn't guarantee absolute certainty that the entire array will perform precisely as predicted. Variations can still occur due to factors such as offset, parasitics, edge effects, defects, crosstalk, and environmental conditions. But if we take care of the matching, offset cancellation, parasitic components, proper layout with the guard ring to isolate pixels, and using calibration, we believe that the results in array-level performance will match simulation results reasonably well.

C. Reconfigurability

The functional model of a retina is largely represented by linear filters, with temporal constants and spatial constants being the most significant factors to reconfigure in order to

TABLE I
COMPARISON OF THIS WORK WITH OTHER SILICON RETINAS.

Type	**[10]**	**[8]**	**[57]**	**[58]**	**[59]**	**[60]**	**This Work**
Year	2006	2007	2010	2010	2014	2017	2022
Functionality	Temporal contrast	Spatial contrast	Temporal contrast	Spatial contrast	Temporal contrast + APS	Spatio-temporal	Spatio-temporal
Technology	0.35μm	0.35μm	0.18μm	0.35μm	0.18μm	+	0.18μm
Pixel complexity	26 transistors, 3C	104 transistors, 1C	77 transistors, 4C,2PD	131 transistors, 2C	47 transistors, 3C	+	83 transistors 5C
Array size	128×128	32×32	304×240	32×32	240×180(DVS) 240×180(APS)	128×128	1 pixel
Pixel size (μm)	40×40	58×56	30×30	81.5×76.5	18.5×18.5	178×154	51×114
Power/pixel	400nW	9.7μW	1.3μW	264nW	347nW	21.7μW	369nW@10nA
Operating regimes	WI	WI	WI	WI	WI	SI	WI
Spatial contrast computation	No	Diffusive grid neighbourhood	No	Diffusive grid neighbourhood	No	Resistive network	Diffusive grid neighbourhood
Design based on	Voltage mode	Current mode	Voltage mode	Current mode	Voltage mode	Voltage mode	Current mode
Hardware	Analog	Analog	Analog	Analog	Analog	Analog and digital FPGA	Analog
Result Type	Measured	Measured	Measured	Measured	Measured	Measured	Measured
Supply voltage (V)	3.3	3.3	1.8 and 3.3	3.3	1.8/3.3	+	1.8
Contrast gain control	No	No	No	No	No	No	Yes
Luminescence adaptation	No	No	No	No	No	No	Yes
Tonic and phasic cells	No	No	No	No	No	No	Yes

+ The works did not include the corresponding values for the designs they presented.

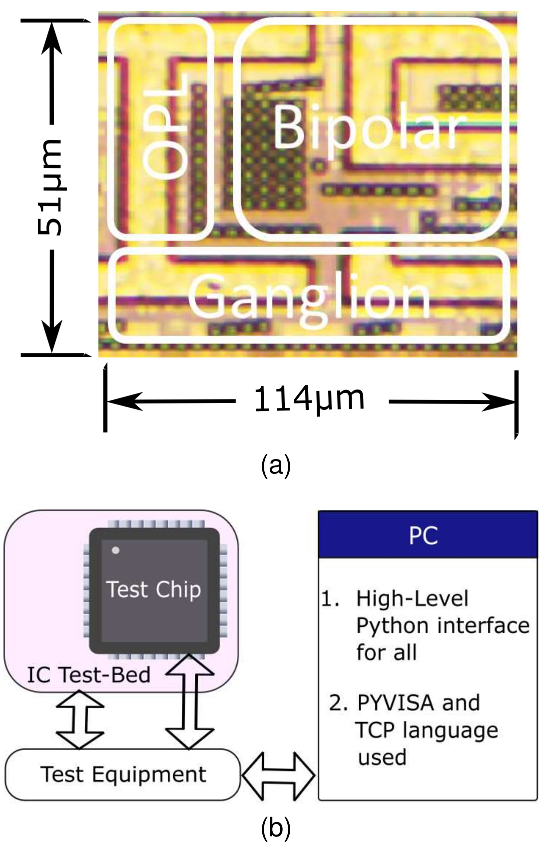

Fig. 14. (a) The die micro-photograph of the fabricated test chip pixel. (b) Measurement setup for the prototyped test chip.

compare different retinas. For example, the cat retina and primate retina have different temporal and spatial constants. The tau-cell filters have the flexibility to adjust the time constants to desired values externally by varying the bias currents. Similarly, the spatial constant of the spatial filter can be adjusted outwardly by bias voltages [32]. This way, the parameters of each retina model can be set on the retina chip.

D. Fill Factor

The number of transistors in this analog retina pixel is more than the standard 3T or 4T CMOS image sensor pixel. Thus it can reduce the fill factor and, thereby, the image quality. This was a common disadvantage in analog retinas due to the large size of retinal processing circuits. This issue can now be overcome by the stacked chip method in which the entire photodiodes are placed on one chip, and the retinal computing circuits are on another chip. There will be interconnections between these two chips. The stacked chip method allows more complex retina models to be implemented while keeping a near 100% fill factor.

E. Comparison

Table I presents a comparison between the measured performance of a tau-cell-based analog silicon retina and designs with comparable characteristics that have been documented in previous literature. By examining the table, we can observe that this particular retina possesses both luminance adaptation and contrast gain control, which is not present in other retinas. These mechanisms are crucial in enabling the retina to process a diverse range of visual inputs. In addition, the table demonstrates that the utilization of tonic and phasic

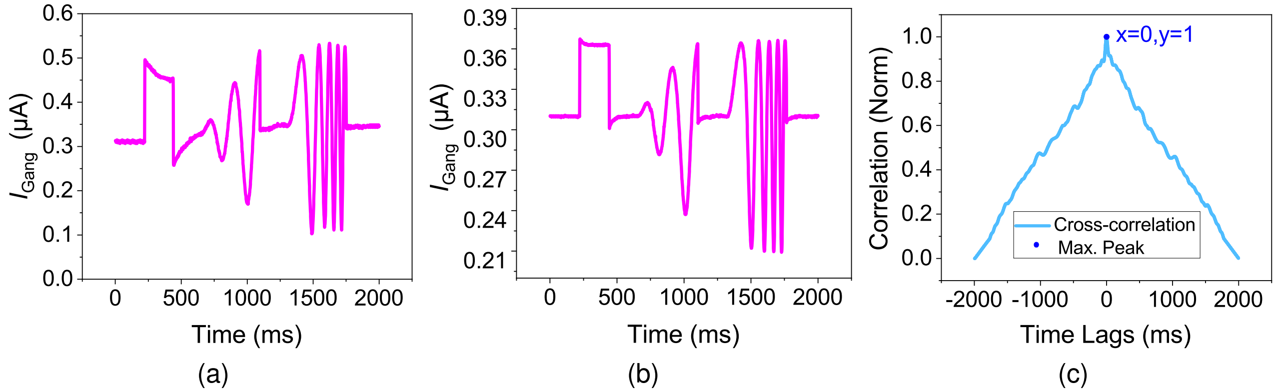

Fig. 15. The measured response of the ganglion current I_{Gang} at two high-pass filter bias currents (I_{tauh}) is depicted for the chirp input signal shown in Fig. 8 where (a) Shows the response for a bias current I_{tauh}=1ρA; (b) Shows the response for a bias current I_{tauh}=5ρA; (c) Depicts the time difference of the measured current I_{Gang} with the software model.

cells within this retina exceeds current standards. Tonic cells preserve a consistent portrayal of a stimulus, while phasic cells demonstrate exceptional ability in detecting changes in the stimulus. This allows the visual system to detect and respond to a wide range of visual stimuli, from low-contrast, slowly moving objects to high-contrast, rapidly changing objects. Table I also shows that the implemented designs consume a minimum number of transistors as compared with spatial contrast retinas. In contrast to other analog silicon retinas, this specific analog retina provides the advantage of reconfigurability. This is important to test or compare other biological retinas.

F. Limitations

The current version of the proposed silicon retina pixel is rectangular, which is unconventional and should be avoided, as it results in different spatial resolutions along the x- and y-axes of the chip. The dimensions of the pixel are large, which will limit the resolution of the image that can be processed. In addition, large pixel arrays have significant parasitic due to the long interconnections (rows or columns), resulting in increased dynamic power consumption. Future versions of the chip will take into consideration these factors and improve the performance and power consumption.

V. Conclusion

In this paper, a novel bio-plausible reconfigurable analog spatio-temporal retina design is presented. Our approach involves taking an established software model of the retina and implementing this in hardware. Building this model from scratch, rather than modifying an existing design, gives us complete control over the selection of building blocks to use. This analog retina incorporates spatio-temporal band-pass filtering in the OPL layer, luminance adaptation, contrast gain control mechanism, tonic and phasic cells, and spiking. The OPL layer filter exhibits a center-surround structure and is a spatially DoG filter with temporal biphasic properties. As a result, this filter can serve as both an edge and movement detector, which is a crucial feature of this retina. To accommodate varying levels of light contrast, the contrast gain control mechanism is incorporated between bipolar and amacrine cells. This mechanism is observed in the biological retina and implemented through current-mode subthreshold MOS circuits, utilizing a novel absolute value circuit. Additionally, luminance adaptation at the photoreceptor level is represented by a high-pass filter. The presence of both tonic and phasic cells in the retina enables a diverse range of visual processing capabilities. This high-performance silicon retina can be utilized in various applications such as retinal prostheses, autonomous vehicles, robots, and mobile devices, to detect objects and track motion within a scene.

Acknowledgment

The authors wish to acknowledge the joint Memorandum of Understanding (MoU) between Indian Institute of Science, Bangalore, and the International Centre for Neuromorphic Systems, Western Sydney University, Australia. This work is supported by Pratiksha Trust (Grant No: FG/SMCH-22-2106).

Conflict of Interest Statement

The authors have no conflicts of interest to disclose.

References

[1] J.-Y. Kim, M. Kim, S. Lee, J. Oh, K. Kim, and H.-J. Yoo, "A 201.4 GOPS 496 mw real-time multi-object recognition processor with bio-inspired neural perception engine," *IEEE Journal of Solid-State Circuits*, vol. 45, no. 1, pp. 32–45, 2009.

[2] Y. Hirano, C. Garcia, R. Sukthankar, and A. Hoogs, "Industry and object recognition: Applications, applied research and challenges," in *Toward category-level object recognition*. Springer, 2006, pp. 49–64.

[3] A. A. Abbo, R. P. Kleihorst, V. Choudhary, L. Sevat, P. Wielage, S. Mouy, B. Vermeulen, and M. Heijligers, "Xetal-ii: a 107 GOPS, 600 mw massively parallel processor for video scene analysis," *IEEE Journal of Solid-State Circuits*, vol. 43, no. 1, pp. 192–201, 2008.

[4] C. A. Mead and M. A. Mahowald, "A silicon model of early visual processing," *Neural networks*, vol. 1, no. 1, pp. 91–97, 1988.

[5] A. G. Andreou and K. A. Boahen, "A 590,000 transistor 48,000 pixel, contrast sensitive, edge enhancing, cmos imager-silicon retina," in *Proceedings Sixteenth Conference on Advanced Research in VLSI*. IEEE, 1995, pp. 225–240.

[6] P.-F. Ruedi, P. Heim, F. Kaess, E. Grenet, F. Heitger, P.-Y. Burgi, S. Gyger, and P. Nussbaum, "A 128× 128 pixel 120 dB dynamic-range vision-sensor chip for image contrast and orientation extraction," *IEEE Journal of Solid-State Circuits*, vol. 38, no. 12, pp. 2325–2333, 2003.

[7] U. Mallik, M. Clapp, E. Choi, G. Cauwenberghs, and R. Etienne-Cummings, "Temporal change threshold detection imager," in *ISSCC. 2005 IEEE International Digest of Technical Papers. Solid-State Circuits Conference, 2005.* IEEE, 2005, pp. 362–603.

[8] J. Costas-Santos, T. Serrano-Gotarredona, R. Serrano-Gotarredona, and B. Linares-Barranco, "A spatial contrast retina with on-chip calibration for neuromorphic spike-based aer vision systems," *IEEE Transactions on Circuits and Systems I: Regular Papers*, vol. 54, no. 7, pp. 1444–1458, 2007.

[9] P. Lichtsteiner, C. Posch, and T. Delbruck, "A 128× 128 120 dB 15 μs latency asynchronous temporal contrast vision sensor," *IEEE Journal of Solid-State Circuits*, vol. 43, no. 2, pp. 566–576, 2008.

[10] C. P. Lichtsteiner, Patrick and T. Delbruck, "A 128 x 128 120 dB 30mw asynchronous vision sensor that responds to relative intensity changen," *International Solid State Circuits Conference-Digest of Technical Papers*, pp. 2060–2069, 2006.

[11] T. Finateu, A. Niwa, D. Matolin, K. Tsuchimoto, A. Mascheroni, E. Reynaud, P. Mostafalu, F. Brady, L. Chotard, F. LeGoff *et al.*, "5.10 a 1280× 720 back-illuminated stacked temporal contrast event-based vision sensor with 4.86 μm pixels, 1.066 geps readout, programmable event-rate controller and compressive data-formatting pipeline," in *2020 IEEE International Solid-State Circuits Conference-(ISSCC)*. IEEE, 2020, pp. 112–114.

[12] M. Guo, S. Chen, Z. Gao, W. Yang, P. Bartkovjak, Q. Qin, X. Hu, D. Zhou, M. Uchiyama, S. Fukuoka *et al.*, "A 3-wafer-stacked hybrid 15mpixel cis+ 1 mpixel evs with 4.6 gevent/s readout, in-pixel tdc and on-chip isp and esp function," in *2023 IEEE International Solid-State Circuits Conference (ISSCC)*. IEEE, 2023, pp. 90–92.

[13] A. Niwa, F. Mochizuki, R. Berner, T. Maruyarma, T. Terano, K. Takamiya, Y. Kimura, K. Mizoguchi, T. Miyazaki, S. Kaizu *et al.*, "A 2.97 μm-pitch event-based vision sensor with shared pixel front-end circuitry and low-noise intensity readout mode," in *2023 IEEE International Solid-State Circuits Conference (ISSCC)*. IEEE, 2023, pp. 4–6.

[14] K. Kodama, Y. Sato, Y. Yorikado, R. Berner, K. Mizoguchi, T. Miyazaki, M. Tsukamoto, Y. Matoba, H. Shinozaki, A. Niwa *et al.*, "1.22 μm 35.6 mpixel rgb hybrid event-based vision sensor with 4.88 μm-pitch event pixels and up to 10k event frame rate by adaptive control on event sparsity," in *2023 IEEE International Solid-State Circuits Conference (ISSCC)*. IEEE, 2023, pp. 92–94.

[15] T. J. Warren, "Mechanisms of lateral-inhibitory feedback from horizontal cells to cone photoreceptors at the first synapse of the retina," 2016.

[16] M. Meister and M. J. Berry, "The neural code of the retina," *neuron*, vol. 22, no. 3, pp. 435–450, 1999.

[17] C. J. Whitmire and G. B. Stanley, "Rapid sensory adaptation redux: a circuit perspective," *Neuron*, vol. 92, no. 2, pp. 298–315, 2016.

[18] M. Ghodrati, E. Zavitz, M. G. Rosa, and N. S. Price, "Contrast and luminance adaptation alter neuronal coding and perception of stimulus orientation," *Nature communications*, vol. 10, no. 1, pp. 1–13, 2019.

[19] I. Ohzawa, G. Sclar, and R. D. Freeman, "Contrast gain control in the cat's visual system," *Journal of neurophysiology*, vol. 54, no. 3, pp. 651–667, 1985.

[20] R. Shapley and C. Enroth-Cugell, "Visual adaptation and retinal gain controls," *Progress in retinal research*, vol. 3, pp. 263–346, 1984.

[21] D. Chander and E. Chichilnisky, "Adaptation to temporal contrast in primate and salamander retina," *Journal of Neuroscience*, vol. 21, no. 24, pp. 9904–9916, 2001.

[22] N. Brenner, W. Bialek, and R. d. R. Van Steveninck, "Adaptive rescaling maximizes information transmission," *Neuron*, vol. 26, no. 3, pp. 695–702, 2000.

[23] A. L. Fairhall, G. D. Lewen, W. Bialek, and R. R. de Ruyter van Steveninck, "Efficiency and ambiguity in an adaptive neural code," *Nature*, vol. 412, no. 6849, pp. 787–792, 2001.

[24] D. L. Ringach and B. J. Malone, "The operating point of the cortex: neurons as large deviation detectors," *Journal of Neuroscience*, vol. 27, no. 29, pp. 7673–7683, 2007.

[25] T. O. Sharpee, H. Sugihara, A. V. Kurgansky, S. P. Rebrik, M. P. Stryker, and K. D. Miller, "Adaptive filtering enhances information transmission in visual cortex," *Nature*, vol. 439, no. 7079, pp. 936–942, 2006.

[26] S. Wang and J. Zhao, "A new prospective on light adaptation of visual system research with the emerging knowledge on non-image-forming effect," *Frontiers in Built Environment*, p. 222.

[27] A. Wohrer and P. Kornprobst, "Virtual retina: a biological retina model and simulator, with contrast gain control," *Journal of computational neuroscience*, vol. 26, no. 2, pp. 219–249, 2009.

[28] C. Mead, "Neuromorphic electronic systems," *Proceedings of the IEEE*, vol. 78, no. 10, pp. 1629–1636, 1990.

[29] C. S. Thakur, R. Wang, T. J. Hamilton, J. Tapson, and A. van Schaik, "A low power trainable neuromorphic integrated circuit that is tolerant to device mismatch," *IEEE Transactions on Circuits and Systems I: Regular Papers*, vol. 63, no. 2, pp. 211–221, 2016.

[30] C. S. Thakur, R. Wang, T. J. Hamilton, R. Etienne-Cummings, J. Tapson, and A. van Schaik, "An analogue neuromorphic co-processor that utilizes device mismatch for learning applications," *IEEE Transactions on Circuits and Systems I: Regular Papers*, vol. 65, no. 4, pp. 1174–1184, 2017.

[31] C. S. Thakur, J. L. Molin, G. Cauwenberghs, G. Indiveri, K. Kumar, N. Qiao, J. Schemmel, R. Wang, E. Chicca, J. Olson Hasler *et al.*, "Large-scale neuromorphic spiking array processors: A quest to mimic the brain," *Frontiers in neuroscience*, vol. 12, p. 891, 2018.

[32] E. A. Vittoz, "Analog vlsi signal processing: Why, where, and how?" *Analog Integrated Circuits and Signal Processing*, vol. 6, no. 1, pp. 27–44, 1994.

[33] J. Huth, T. Masquelier, and A. Arleo, "Convis: A a Toolbox To Fit and Simulate Filter-based Models of Early Visual Processing," *Frontiers in neuroinformatics*, vol. 12, p. 9, 2018.

[34] S.-C. Liu, J. Kramer, G. Indiveri, T. Delbrück, and R. Douglas, *Analog VLSI: circuits and principles*. MIT press, 2002.

[35] A. van Schaik and C. Jin, "The tau-cell: a new method for the implementation of arbitrary differential equations," in *Proceedings of the 2003 International Symposium on Circuits and Systems, 2003. ISCAS'03.*, vol. 1. IEEE, 2003, pp. I–I.

[36] A. Schaik, R. Reeve, C. Jin, and T. Hamilton, "An avlsi cricket ear model," *Advances in Neural Information Processing Systems*, vol. 18, 2005.

[37] T. J. Hamilton, C. Jin, and A. van Schaik, "An analysis of matching in the tau cell log-domain filter," in *2006 IEEE International Symposium on Circuits and Systems*. IEEE, 2006, pp. 4–pp.

[38] G. Indiveri, B. Linares-Barranco, T. J. Hamilton, A. Van Schaik, R. Etienne-Cummings, T. Delbruck, S.-C. Liu, P. Dudek, P. Häfliger, S. Renaud *et al.*, "Neuromorphic silicon neuron circuits," *Frontiers in neuroscience*, vol. 5, p. 73, 2011.

[39] A. van Schaik and C. Jin, "The tau-cell: a new method for the implementation of arbitrary differential equations," in *Proceedings of the 2003 International Symposium on Circuits and Systems, 2003. ISCAS '03.*, vol. 1, 2003, pp. I–I.

[40] A. Wohrer, "Model and large-scale simulator of a biological retina, with contrast gain control," Ph.D. dissertation, Université de Nice-Sophia Antipolis, 2008.

[41] J. Fernández-Berni, R. Carmona-Galán, R. d. Río, R. Kleihorst, W. Philips, and Á. Rodríguez-Vázquez, "Focal-plane sensing-processing: A power-efficient approach for the implementation of privacy-aware networked visual sensors," *Sensors*, vol. 14, no. 8, pp. 15 203–15 226, 2014.

[42] J. Fernández-Berni and R. Carmona-Galán, "All-mos implementation of rc networks for time-controlled gaussian spatial filtering," *International Journal of Circuit Theory and Applications*, vol. 40, no. 8, pp. 859–876, 2012.

[43] M. Suarez, V. M. Brea, J. Fernandez-Berni, R. Carmona-Galan, D. Cabello, and A. Rodriguez-Vazquez, "Low-power cmos vision sensor for gaussian pyramid extraction," *IEEE Journal of Solid-State Circuits*, vol. 52, no. 2, pp. 483–495, 2016.

[44] C. S. Thakur, J. Molin, and R. Etienne-Cummings, "Real-time image segmentation using a spiking neuromorphic processor," in *2017 51st Annual Conference on Information Sciences and Systems (CISS)*. IEEE, 2017, pp. 1–6.

[45] E. A. Vittoz, "Pseudo-resistive networks and their applications to analog collective computation," in *International Conference on Artificial Neural Networks*. Springer, 1997, pp. 1131–1150.

[46] R. Boitard, M. T. Pourazad, P. Nasiopoulos, and J. Slevinsky, "Demystifying high-dynamic-range technology: A new evolution in digital media," *IEEE Consumer Electronics Magazine*, vol. 4, no. 4, pp. 72–86, 2015.

[47] R. M. Shapley and J. D. Victor, "The effect of contrast on the transfer properties of cat retinal ganglion cells." *The Journal of physiology*, vol. 285, no. 1, pp. 275–298, 1978.

[48] S. A. Baccus and M. Meister, "Fast and slow contrast adaptation in retinal circuitry," *Neuron*, vol. 36, no. 5, pp. 909–919, 2002.

[49] J. D. Victor, "The dynamics of the cat retinal x cell centre." *The Journal of physiology*, vol. 386, no. 1, pp. 219–246, 1987.

[50] C. Enroth-Cugell and A. W. Freeman, "The receptive-field spatial structure of cat retinal y cells." *The Journal of Physiology*, vol. 384, no. 1, pp. 49–79, 1987.

[51] A. Van Schaik, C. Jin, A. McEwan, T. J. Hamilton, S. Mihalas, and E. Niebur, "A log-domain implementation of the mihalas-niebur neuron model," in *Proceedings of 2010 IEEE International Symposium on Circuits and Systems*. IEEE, 2010, pp. 4249–4252.

[52] J. Schnapf, B. Nunn, M. Meister, and D. Baylor, "Visual transduction in cones of the monkey macaca fascicularis." *The Journal of physiology*, vol. 427, no. 1, pp. 681–713, 1990.

[53] A. Van Schaik, "Building blocks for electronic spiking neural networks," *Neural networks*, vol. 14, no. 6-7, pp. 617–628, 2001.

[54] J. Huth, T. Masquelier, and A. Arleo, "A retina model based on convolutions on the gpu," *bioRxiv*, p. 169284, 2017.

[55] Z. Wang, A. C. Bovik, H. R. Sheikh, and E. P. Simoncelli, "Image quality assessment: from error visibility to structural similarity," *IEEE transactions on image processing*, vol. 13, no. 4, pp. 600–612, 2004.

[56] J.-C. Yoo and T. H. Han, "Fast normalized cross-correlation," *Circuits, systems and signal processing*, vol. 28, no. 6, pp. 819–843, 2009.

[57] C. Posch, D. Matolin, and R. Wohlgenannt, "A qvga 143 dB dynamic range asynchronous address-event pwm dynamic image sensor with lossless pixel-level video compression," in *2010 IEEE International Solid-State Circuits Conference-(ISSCC)*. IEEE, 2010, pp. 400–401.

[58] J. A. Leñero-Bardallo, T. Serrano-Gotarredona, and B. Linares-Barranco, "A five-decade dynamic-range ambient-light-independent calibrated signed-spatial-contrast aer retina with 0.1-ms latency and optional time-to-first-spike mode," *IEEE Transactions on Circuits and Systems I: Regular Papers*, vol. 57, no. 10, pp. 2632–2643, 2010.

[59] C. Brandli, R. Berner, M. Yang, S.-C. Liu, and T. Delbruck, "A 240$\times$180 130-dB 3 μs latency global shutter spatiotemporal vision sensor," *IEEE Journal of Solid-State Circuits*, vol. 49, no. 10, pp. 2333–2341, 2014.

[60] Y. Hayashida, Y. Kudo, R. Ishida, H. Okuno, and T. Yagi, "Retinal circuit emulator with spatiotemporal spike outputs at millisecond resolution in response to visual events," *IEEE transactions on biomedical circuits and systems*, vol. 11, no. 3, pp. 597–611, 2017.

Prince Philip (Student Member, IEEE) is a Ph.D. student in the NeuRonICS Laboratory, Department of Electronic Systems Engineering, at the Indian Institute of Science in Bangalore, India. Before joining the NeuRonICS Lab, he worked in the areas of analog/digital and radio frequency integrated circuits in industry and academia. He graduated in Electronics and Communication Engineering from Visvesvaraya Technological University in Karnataka, India. His current research interests include neuromorphic engineering, bio-inspired vision sensors, analog and digital integrated circuits, and signal processing.

Kapil Jainwal (Member, IEEE) received Ph.D. from Electrical Engineering Department, Indian Institute of Technology (IIT) Delhi, India in 2019 and M.Tech. degree from IIT Bombay, India, in 2008. Currently he is working as Assistant professor in Electrical Engineering Department, IIT Hyderabad. Before IIT Hyd, he worked with Samsung R&D, Bangalore, India. His professional interests include analog/mixed-mode integrated circuits and CMOS image sensors.

André van Schaik (Fellow, IEEE) is a pioneer in Neuromorphic Engineering and the director of the International Centre for Neuromorphic Systems at the Western Sydney University. He received his M.Sc. degree in electrical engineering from the University of Twente, Enschede, The Netherlands, in 1990 and his PhD degree in neuromorphic engineering from the Swiss Federal Institute of Technology (EPFL) Lausanne, Switzerland, in 1998. From 1991 until 1994, he was a researcher at the Swiss Centre for Electronics and Microtechnology (CSEM), where he developed the first commercial neuromorphic chip – the optical motion detector used in Logitech trackballs. In 1998 he was a postdoctoral research fellow in the Department of Physiology at the University of Sydney, and in 1999 he became a Senior Lecturer in their School of Electrical and Information Engineering and a Reader in 2004. In 2011 he became a full Professor at Western Sydney University. His research focuses on all aspects of neuromorphic engineering, encompassing neurophysiology, computational neuroscience, software and algorithm development, and electronic hardware design. He is a Fellow of the IEEE for contributions to Neuromorphic Circuits and Systems. He has authored more than 200 papers and is an inventor of more than 35 patents. In addition, he has founded three technology start-ups

Chetan Singh Thakur (Senior Member, IEEE) received the Ph.D. degree in neuromorphic engineering from the MARCS Research Institute, Western Sydney University, in 2016, and the M.Tech degree from the Indian Institute of Technology, Bombay, India, in 2007. He was a Post-Doctoral Researcher with Johns Hopkins University, Baltimore, MD, USA. He also worked as a Senior Integrated Circuit Design Engineer at Texas Instruments Singapore for few years. In 2017, he joined the Indian Institute of Science, Bangalore, and he is now working as an Associate Professor. His research interests include the computing principles of the brain and apply those to build novel intelligent VLSI systems. He received several awards, such as the Pratiksha Trust Young Investigator Award, the Abdul Kalam Innovation Award from the Indian National Academy of Engineering (INAE) and the Inspire Faculty Award for brain-inspired computing from the Department of Science and Technology (DST).